

Computational fluid dynamics prediction of marine propeller cavitation including solution verification

Thomas Lloyd¹, Guilherme Vaz¹, Douwe Rijpkema¹, Antoine Reverberi^{2,3}

{t.lloyd; g.vaz; d.r.rijpkema}@marin.nl; antoine.reverberi@eleves.ec-nantes.fr

¹ MARIN, Wageningen, NL; ² MARIN Academy, Wageningen, NL; ³ École Centrale de Nantes, Nantes, FR.

ABSTRACT

This paper analyses the effect of grid refinement on computational fluid dynamics simulations of cavitating propeller flow. Refinement is made both globally, using geometrically similar grids, and locally, by applying adaptive grid refinement. The test case is the E779A propeller operating in uniform inflow conditions in a cavitation tunnel. This allows more computationally efficient steady simulations to be made, permitting a grid uncertainty analysis not previously seen for cavitating flow computations. Unsteady simulations are also presented in order to compare two turbulence modelling approaches. Differences in the discretisation uncertainty in terms of propeller thrust and torque were found to be small between wetted and cavitating flow conditions, although the order of convergence for the cavitating case is lower. Overall the largest effect of grid refinement is found to be in the tip vortex region, where differences in the predicted cavity extents are significant between grids. The use of adaptive grid refinement allows improved capture of tip vortex cavitation with fewer total grid cells, although the cavity extent is limited by increasing eddy viscosity when using RANS. Application of DDES reduces this influence somewhat, motivating further study into the potential of scale-resolving simulations in combination with adaptive grid refinement for vortex cavitation prediction.

Keywords

RANS; DDES; verification; cavitation; adaptive grid refinement

1 INTRODUCTION

Computational prediction of marine propeller cavitation is an important area of research aimed at improving propeller performance, in terms of efficiency, noise characteristics and erosion. However, computational fluid dynamics (CFD) simulations of cavitation are complicated somewhat, when compared to wetted flow, due to a strong interaction between numerical aspects such as grid density and timestep, as well as cavitation and turbulence model. One particularly challenging phenomenon to model is tip vortex cavitation (TVC), where the (in)ability of commonly-used engineering approaches such as Reynolds-averaged

Navier-Stokes (RANS) simulations to capture the tip vortex flow correctly has been widely addressed in literature. For example, Decaix et al. (2015) had to lower the simulated cavitation number when using RANS in order to capture TVC of a foil. This was attributed to the pressure drop in the vortex core being underestimated. Wang et al. (2015) recommended using a non-linear two-equation RANS model in order to correctly resolve a cavitating tip vortex. Gaggero et al. (2014) meanwhile concluded that grid resolution was more important than cavitation model parameters when predicting inception of TVC, and that RANS can be a satisfactory design tool for engineering purposes.

Non-cavitating tip vortex flows have also been studied, with the aim of identifying cavitation inception. Asnaghi et al. (2016) showed that applying curvature correction to a RANS model does not lead to improvement in non-cavitating tip vortex prediction, while recommending grid cell sizes of 20 and 40 times the Kolmogorov scale in the in-plane and streamwise directions respectively. Yvin & Muller (2016) used the pressure Hessian as criterion for adaptive grid refinement (AGR) in order to correctly capture the minimum pressure in the tip vortex core. It was found that a large number of additional cells are required in order to obtain convergence, although it is expected that this requirement will be reduced for cavitating vortices, where the minimum pressure inside the vortex core is limited after inception. Similarly Windt & Bosschers (2015) performed a grid refinement study for a non-cavitating propeller, finding very high uncertainty for the minimum pressure inside the vortex core. Application of *a-priori* AGR allowed similar results to be obtained compared to the original grid set, but with three times fewer total grid cells. No grid independent solution could be obtained when using AGR however.

The aim of this study is to analyse the effect of grid density and topology on CFD predictions of cavitating propeller flow. We extend previous work on solution verification for non-cavitating propellers (Lloyd et al., 2015; Rijpkema & Vaz, 2011) and adaptive grid refinement of propeller tip vortices (Windt & Bosschers, 2015), to cavitating condi-

tions. A simple test case is chosen in order to focus on the effect of grid resolution. Comparison is also made with wetted flow results for the same case in order to differentiate numerical requirements specifically related to cavitating flow.

The paper assumes the following layout. In §2, we outline the key details of the numerical approach. Next, in §3, an overview of the test case setup is given. The results are divided into three main sections: §4 deals with propeller performance prediction including uncertainty analysis; in §5 the effect of grid refinement on flow resolution is discussed; and §6 concerns with the application of adaptive grid refinement. Finally, conclusions and recommendations for future work are presented in §7.

2 NUMERICAL METHODS

2.1 Hydrodynamic flow solver

We solved the governing flow equations using the computational fluid dynamics (CFD) code *ReFresco*¹ (version 2.3.0), developed by MARIN in collaboration with several universities, and already extensively applied to marine propeller flows (Lloyd et al., 2015; Rijpkema et al., 2015; Windt & Bosschers, 2015). The code adopts a finite volume face-based approach, permitting the use of grid cells with an arbitrary number of faces, which eases the gridding of complex engineering geometries. Flow variables are colocated at cell centres, and the equations coupled using a segregated SIMPLE-type solution algorithm. Parallelisation is achieved using MPI and domain decomposition.

For open water propeller RANS computations it is possible to perform steady simulations assuming rotationally symmetric flow. We did this using the *absolute frame of motion* approach in which the governing equations are solved in the body-fixed frame of reference, with the flow variables defined in the earth-fixed frame. This results in a grid velocity term in the continuity equation and *l.h.s.* of the momentum equations and a body-force term on the *r.h.s.* of the momentum equations. For unsteady computations, time stepping was achieved using an first-order implicit scheme. We performed primarily wetted and cavitating flow Reynolds-averaged Navier-Stokes (RANS) computations, using the $k - \sqrt{k}L$ model for turbulence (Menter et al., 2006). In our experience this model gives similar results to the $k - \omega$ SST 2003 model, and is preferred due to the reduction in eddy viscosity and improved convergence behaviour it offers (Rijpkema et al., 2015). For the steady computations presented here, all the turbulence is modelled. In addition, several computations were made using delayed detached eddy simulation (DDES, Gritskevich et al., 2012), based on the $k - \omega$ SST model, where part of the turbulence spectrum is resolved depending on grid density and turbulence length scale.

Cavitation was modelled by adopting a homogeneous

mixture-based approach. A transport equation for the vapour volume fraction α_v is solved, where the liquid (l) and vapour (v) volume fractions are defined such that $\alpha_l + \alpha_v = 1$. The local values of the fluid properties (ρ and μ) then enter into the continuity and momentum equations as a linear blending of the liquid and vapour values, based on the cell value of α_v . The formulation of the source term in the transport equation for α_v was based on that of Sauer & Schnerr (2001); that is, proportional to the square root of the pressure difference $p - p_v$, where p and p_v are the local and vapour pressures respectively. Inception is assumed to occur for $p < p_v$. For steady simulations the cavitation model predicts cavitation extents only; it is assumed that the processes of creation and destruction of the vapour are stationary in space and time, and will therefore not affect the macroscale prediction of the cavity extent. This approach would of course not be appropriate for studies related to pressure pulses, noise or erosion.

All flow variables were discretised in space using second-order schemes, except for the convective flux of the turbulence and cavitation quantities which were treated using a first-order upwind scheme.

2.2 Uncertainty analysis procedure

Verification concerns the uncertainty analysis of a numerical solution, with the aim of evaluating the magnitude of the numerical errors in order to be able to judge the quality of the numerical results. Here it is assumed that the dominant numerical error is the *discretisation* error (that due to the finite spatial and temporal representation of the flow solution), thereby implying that the *iterative* and *round-off* errors are negligible. The reader is referred to Eça & Hoekstra (2014) for full details of the method used here, which requires results from a series of (at least four) geometrically similar computational grids, and estimates the (discretisation) uncertainty (U_{num}) and order of convergence (p_{num}). We have previously applied this approach for non-cavitating propellers; see Lloyd et al. (2015) and Rijpkema & Vaz (2011) for details.

3 TEST CASE SETUP

3.1 Case overview

The propeller considered in this work is the INSEAN E779A, which is widely used for computational test cases due to the availability of large amounts of experimental data (see *e.g.* Salvatore, 2007). Particulars of the case are summarised in Table 1, which corresponds to measurements made in a cavitation tunnel. The advance ratio and cavitation number are defined as $J = U_0/nD$ and $\sigma_n = 2(p_0 - p_v)/\rho_l n^2 D^2$, where U_0 and p_0 are the reference velocity and pressure, and n and D are the propeller rotation rate and diameter.

Note that the results presented here are corrected to approximate open water conditions by multiplying all forces and moments by a factor of 0.98 in order to account for tunnel

¹www.refresco.org

blockage (as was carried out for the experimental values in Salvatore (2007)). No roughness was applied to the leading edges of the blades in the experiments.

Table 1: Details of E779A propeller and test case.

parameter	symbol	value	unit
no. of blades	Z	4	-
propeller diameter	D	0.227	m
expanded area ratio	A_E/A_0	0.689	-
rotation rate	n	36	rpm
inflow speed	U_0	5.8182	$m.s^{-1}$
advance ratio	J	0.71	-
cavitation number	σ_n	1.763	-
Reynolds number	$Re_{0.7R}$	1.6×10^6	-

The cavitation pattern observed in the experiment is shown in Figure 1, exhibiting sheet, tip vortex and hub vortex cavitation.

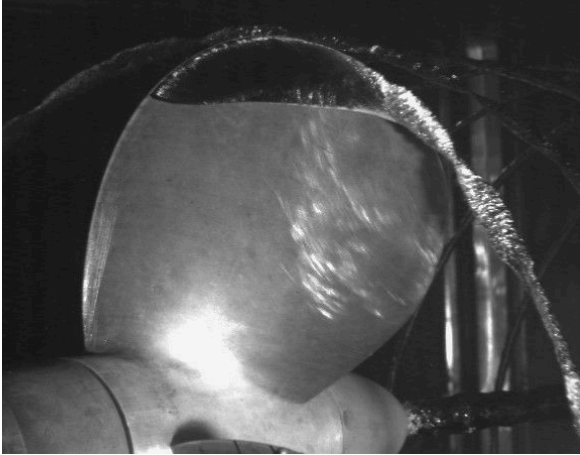


Figure 1: Cavitation observation for chosen test case condition: $J = 0.71$; $\sigma_n = 1.763$ (Salvatore, 2007).

3.2 Computational settings

The fluid properties (density and dynamic viscosity) of the liquid and vapour phases were specified as $(\rho_l, \rho_v) = (998, 0.017) \text{ kgm}^{-3}$ and $(\mu_l, \mu_v) = (1.008 \times 10^{-3}, 1.02 \times 10^{-5}) \text{ kgm}^{-1}\text{s}^{-1}$. Turbulence kinetic energy and eddy viscosity were set at the inlet to replicate a turbulence intensity of 2%, as measured in the cavitation tunnel. For cavitating cases, the cavitation number was fixed by setting $p_0 = 0$ and modifying p_v accordingly. In order to help with convergence of the steady simulations, the flow was initialised from the wetted flow solution and p_v updated in stages until the correct σ_n was achieved. The model parameter in the Sauer cavitation model corresponding to number of nuclei was set to 10^8 .

3.3 Domain design

A cylindrical domain was used, with a cross-section area equivalent to the cavitation tunnel, and is the same as that

reported in Vaz et al. (2015). The domain length upstream and downstream of the propeller are $2.4D$ and $4D$ respectively, while the domain radius is $1.47D$. The following boundary conditions were used (corresponding to the colours shown in Figure 2). Propeller blades and hub were treated as rotating walls (purple) with the propeller shaft assumed to be a non-rotating wall (grey). At the inlet a uniform velocity inflow was prescribed (red). The two outlet boundaries consist of an inner part where an outflow condition was used (yellow) and an outer part specified as fixed zero pressure (green). Finally, the outer boundary was treated as a slip wall (blue), as an approximation of the cavitation tunnel walls.

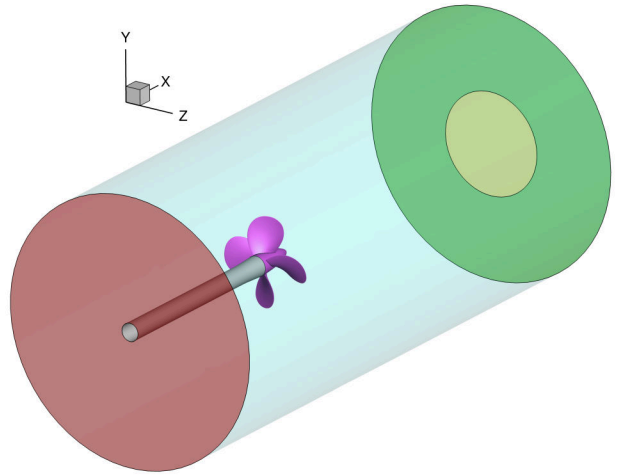


Figure 2: Domain for E779A propeller in cavitation tunnel.

3.4 Grid generation

Generation of a series of geometrically similar grids was carried out using a structured grid generator, by successively coarsening the finest grid by a factor of 1.25. This has the advantages that the grids typically exhibit better iterative convergence behaviour than unstructured grids and are more suitable for use with the discretisation uncertainty analysis procedure used here. A maximum value of the normalised wall-normal first grid cell height, y_{max}^+ , equal to unity was targetted for the coarsest grid. Table 2 provides an overview of the resulting number of cells for each grid.

Table 2: Summary of propeller grid characteristics

grid	cells / $\times 10^{-6}$	faces/blade / $\times 10^{-3}$	y_{max}^+
G6	0.4	3	1.0
G5	1.2	6	0.8
G4	2.8	10	0.6
G3	8.6	21	0.5
G2	14.3	29	0.4
G1	29.9	48	0.3

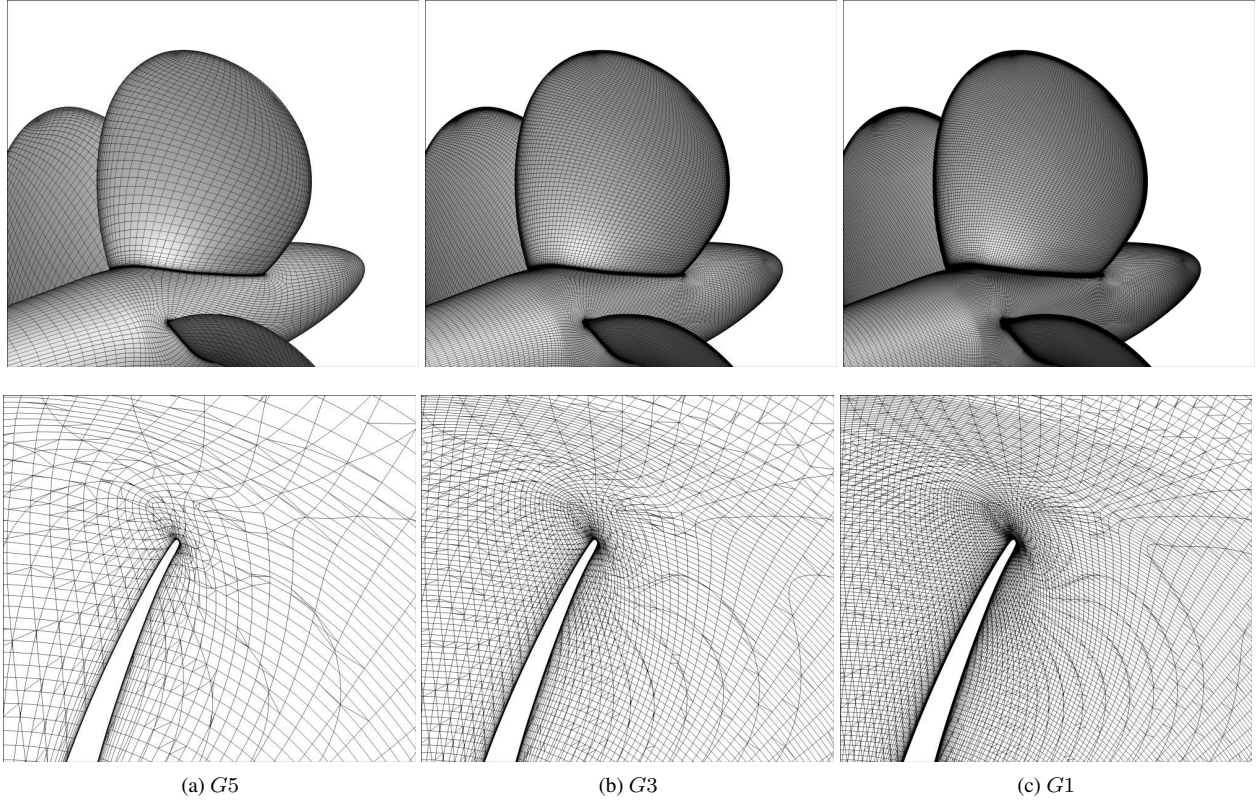


Figure 3: Views of the grids used: surface grid on propeller blades and shaft (top); and axial slice at $x/D = 0.05$ (bottom).

The grids are visualised in Figure 3, in which examples are given of coarse, medium and fine grids. It is noted that in the blade tangential direction, refinement was focussed on accurate capture of the geometry as well as the leading edge suction peak, resulting in clustering at the blade edges. No specific refinement was made for cavitation or tip vortex resolution, with the same topology used as in our previous work on open water non-cavitating conditions (Lloyd et al., 2015); the same grids were used for wetted and cavitating flow computations.

4 PERFORMANCE PREDICTION

The convergence of the computations varied depending on the grid density and flow type. In general, all (steady) wetted flow computations achieved a L_2 -norm residual below 10^{-7} for all flow variables, while this was only 10^{-3} for (steady and unsteady) cavitating flow computations. In this case the iterative convergence of the forces were checked and found to be satisfactory. Propeller performance prediction is evaluated using the thrust and torque coefficients, and open water efficiency, given as

$$K_T = \frac{T}{\rho_l n^2 D^4}, \quad K_Q = \frac{Q}{\rho_l n^2 D^5}, \quad \eta_O = \frac{J}{2\pi} \frac{K_T}{K_Q}, \quad (1)$$

where T and Q are thrust and torque respectively.

4.1 Uncertainty analysis

Results of the uncertainty analysis for both wetted and cavitating flow conditions are presented in Table 3, along with the comparison error E for grid $G3$, which is simply the

percentage difference between the measured and computed values. This can be used to perform a full validation of the results, although this has not been included here since the uncertainty of the measurements was not known.

For the wetted flow case, no directly comparable experimental result exists. Therefore the comparison error was computed for a condition having the same rotation rate but higher cavitation number ($\sigma_n = 2.775$), which was not entirely cavitation free. The computed comparison errors are therefore only given as an indication of the range of deviation between calculated and measured propeller performance. We note however that the results obtained here are within 1% of those we reported previously for the same test case using a different grid (Vaz et al., 2015).

The comparison error for the cavitating case was computed using the data for the same condition reported in Salvatore (2007). It is observed that the differences between calculated and measured values for the cavitating case are small, with a maximum of 5.4% for the thrust coefficient. These values are similar to what we previously reported for the same propeller in wetted flow open water conditions (Lloyd et al., 2015).

Looking solely at the data related to verification, a direct comparison can be made between the wetted and cavitating flow conditions. Overall we observe low uncertainties for both wetted and cavitating results, of around 1% or less. The main difference between the two cases is the order of convergence, which is lower for cavitating flow than wetted flow. Considering that the highest expected

Table 3: Comparison error and uncertainty analysis of propeller performance coefficients for wetted and cavitating flow. The quoted values for E and U_{num} are derived for $G3$.

condition	$E/\%$			$p_{num}/-$			$U_{num}/\%$		
	K_T	$10K_Q$	η_O	K_T	$10K_Q$	η_O	K_T	$10K_Q$	η_O
wetted	-7.6	-9.4	2.0	1.6	2.0	2.0	1.0	1.1	0.8
cavitating	-5.4	-2.7	0.5	1.0	1.7	2.0	0.9	0.7	0.4

value is $p_{num} = 2$, the wetted flow computations exhibit a very good convergence behaviour, although thrust converges more slowly than torque, due to the fact that the grid sensitivities mainly occur close to the blade tip.

4.2 Propeller loading

The low uncertainty can be explained by looking at the radial distribution of the thrust coefficient, which is shown in Figure 4. This is defined as

$$f_x(r/R) = \frac{\Delta F_x/(r/R)}{\rho_l n^2 D^4}, \quad (2)$$

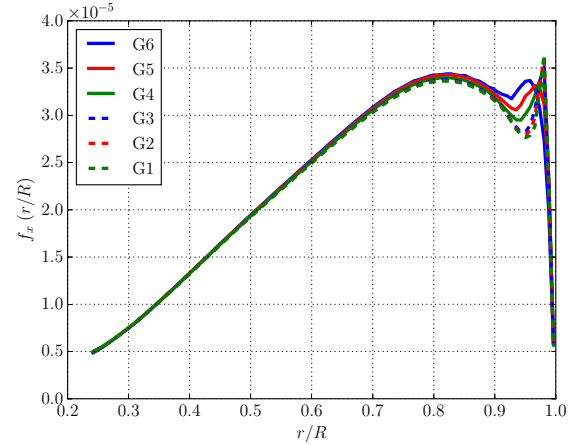
where $\Delta F_x(r/R)$ is the thrust contribution from a radial element of thickness $\Delta r/R$ at radius r/R , R being the propeller tip radius. Integrating this quantity in the radial direction yields the blade thrust.

For the wetted flow case, the main differences are seen close to the blade tip; here the resolution of the leading edge vortex improves with grid refinement, thereby modifying the pressure distribution and radial loading distribution. Little difference is observed between grids $G3$ and $G1$ however. For the cavitating flow prediction the influence of grid refinement is even less, resulting in the (slightly) lower uncertainty figure. Figure 5 compares the two flow conditions predicted using $G3$, where the reduction in tip loading for the cavitating case is clear. This is primarily due to the lower strength of the suction peak and leading edge vortex due to the presence of sheet cavitation. Although the suction peak close to the tip is absent compared to the wetted flow condition, a larger lower pressure area exists due to the cavity. This can be seen by comparing the examining the surface pressure distribution for wetted and cavitating conditions, defined as

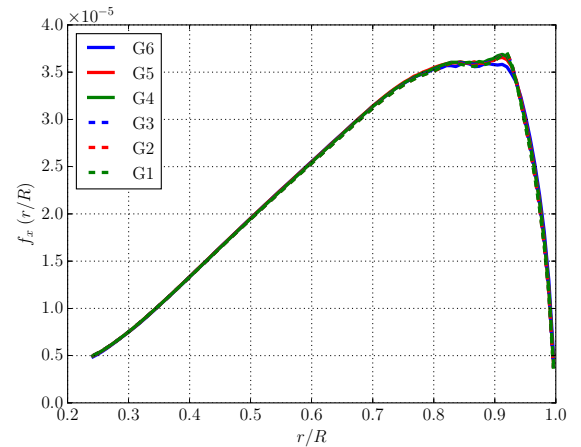
$$C_{pn} = \frac{2(p - p_0)}{\rho_l n^2 D^2}. \quad (3)$$

These are shown for the entire blade and a radial section at $r/R = 0.9$ in Figures 6 and 7.

The net effect of this is an increase in the predicted thrust (and torque) for the cavitating propeller, which is the opposite trend to the measured values, and seems rather counter-intuitive. This is related to the overprediction of the sheet cavity extent compared to the experiments (compare Figures 8 and 1), an issue related to assumptions in the flow modelling, as well as the lack of leading edge roughness used in the experiments (see Reverberi et al., 2016, for further discussion).



(a) wetted



(b) cavitating

Figure 4: Comparison of radial thrust loading for all grids.

5 FLOW PREDICTION

5.1 Vapour volume uncertainty analysis

Next we examine the effect of grid refinement on the cavitating flow prediction. A global view of the cavitation prediction is shown in Figure 8, for three grids of increasing density. The successive relative change in the representative cell size between each grid shown is approximately 1.5. The form of the sheet cavity does not appear sensitive to grid refinement, which can be expected given the low grid uncertainty of the thrust, which is directly related to the pressure distribution on the blade. The tip vortex cavity however exhibits a large grid dependency; for $G5$ no noticeable tip vortex cavitation exists; for $G3$ the tip vortex

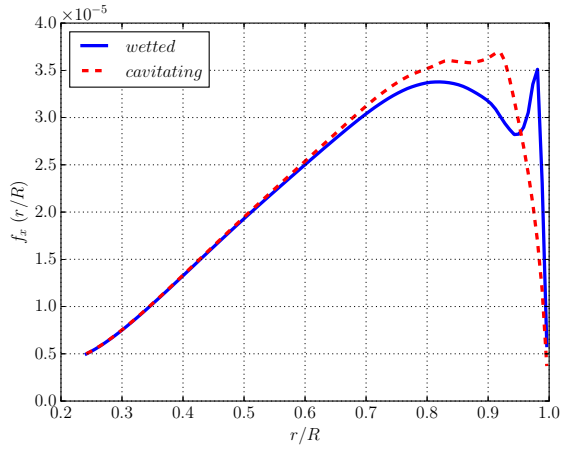


Figure 5: Comparison between radial thrust loading for wetted and cavitating flow conditions, computed using $G3$.

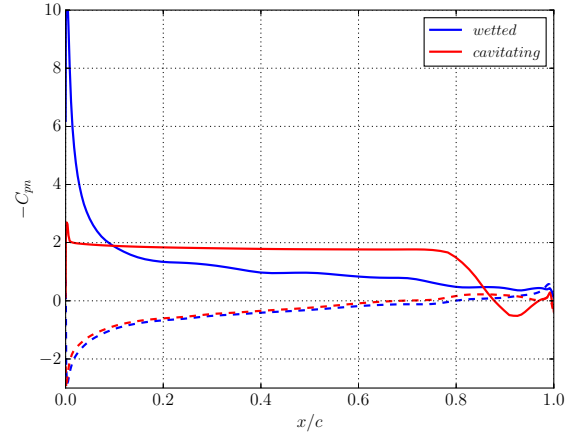
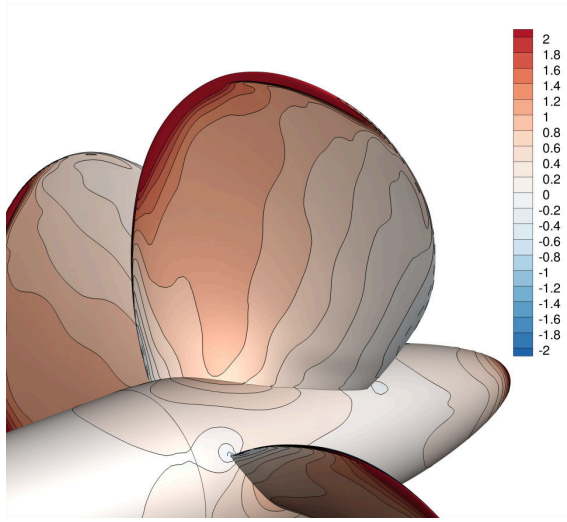
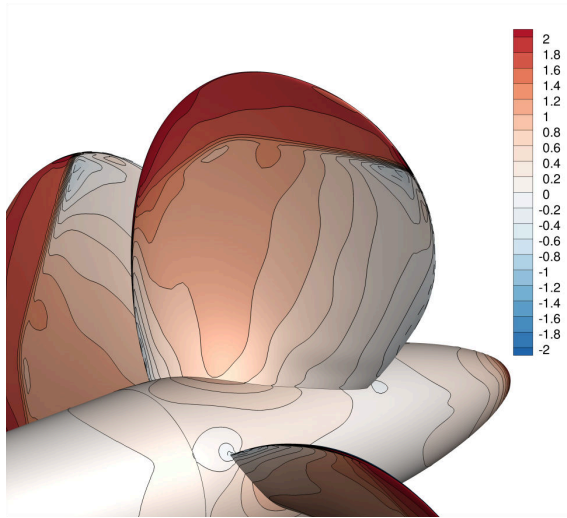


Figure 7: Comparison between chordwise pressure distribution at $r/R = 0.9$ for wetted and cavitating flow using $G3$: Solid - suction side; dashed - pressure side.



(a) wetted



(b) cavitating

Figure 6: Propeller surface pressure distribution $-C_{pm}$ for wetted and cavitating flow conditions, computed using $G3$.

begins to cavitate; and for $G1$ the extension of the cavity increases. The finest grid predicts the characteristic “necked” appearance of the vortex cavity (see Figure 1 for comparison), which is due to the roll-up of the vortex, although the roll-up itself is not clearly seen in the simulation.

Table 4: Uncertainty analysis results for different types of cavitation, neglecting $G6$. Uncertainty values given for $G3$. 1/2 denotes mixed first/second-order grid convergence.

type	quantity	$p_{num}/-$	$U_{num}/\%$
total		1/2	99
sheet		0.8	15
tip	volume	2.0	206
	extent	2.0	88
hub	volume	1.0	41
	extent	1.9	10

In order to quantify the effect of grid refinement on prediction of the different types of cavitation, the same uncertainty analysis procedure used in Section 4 was applied to the integrated vapour volume (for one blade) for sheet, tip vortex and hub vortex cavitation, as well as the combined total. The axial extent of the tip and hub vortex cavity was identified using the isosurfaces shown in Figure 8, while the differentiation between sheet and tip vortex was made at $x_0/D = 0.0374$, the axial location at which no attached cavitation was seen for $G3$. The results of this analysis are given in Table 4. It can be seen that the uncertainty values associated with both the volume and extent of the tip vortex cavity are much higher than for the other types of cavitation, revealing that much finer grids are needed to resolve this sufficiently.

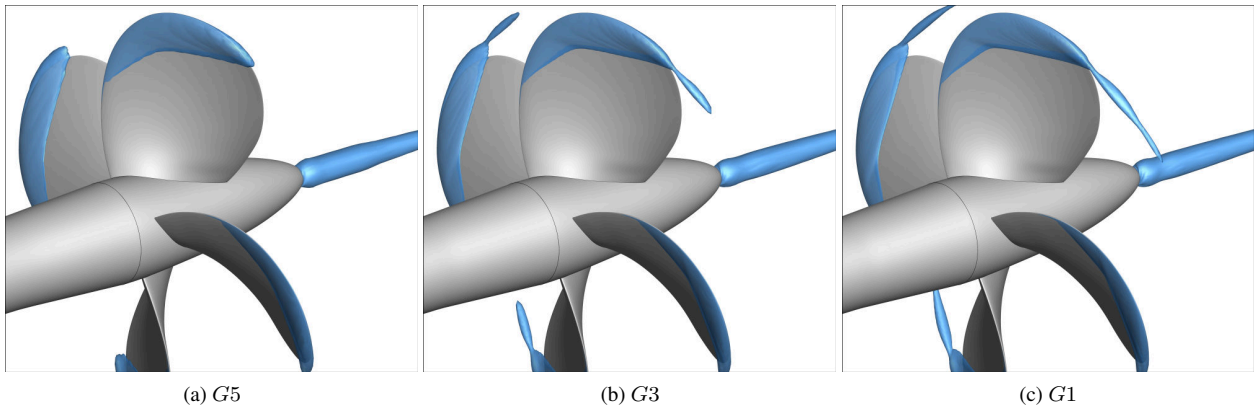


Figure 8: Cavity extents for three different grids visualised using isosurfaces of the vapour volume fraction $\alpha_v = 0.1$.

5.2 Cavitating flow field analysis

Although the predicted shape of the sheet cavity does not appear to change significantly with grid refinement, the variation of the vapour volume fraction on a two-dimensional circumferential slice through the blade reveals more profound differences. Figure 9 shows contours of the vapour volume fraction at a non-dimensional blade radius of $r/R = 0.9$ for three grids of increasing density. The main differences are seen in the sharpness of the liquid-vapour interface, and the resolution of the re-entrant jet. For the finest grid considered here, a much larger region of higher α_v is seen close to the blade, while the tail of the cavity becomes further separated from the blade surface. This is expected to have an effect on the shedding behaviour of the sheet cavity; although not part of the present study, this has been addressed elsewhere (Negrato et al., 2017).

Further analysis of the effect of grid refinement on the cavitating tip vortex is made in Figure 10, where slices of the vapour volume fraction, pressure coefficient and normalised eddy viscosity μ_t/μ are shown at an axial station in the propeller wake, $0.05D$ downstream of the propeller plane. In Figure 10a, the presence of the elongated tip vortex cavity is confirmed, while a much higher vapour concentration is seen for $G1$ than $G3$; thus if a different (higher) value for the isosurface of α_v were used, the difference in the cavity extents would appear much greater.

The pressure field contour exhibits the same overall form for all three grids, although clearly the low pressure region is more extensive for finer grids, and the minimum pressure lower. Referring to the black and white isolines shown in the figure, which represent $\alpha_v = 0.1$ and $C_{pn} = -\sigma_n$ respectively, it is also observed that the size of the region where $p < p_v$ grows more quickly than the cavity extent as the grid is refined.

The final quantity to be analysed is the eddy viscosity ratio, which is an indication of the additional dissipation added by the turbulence model. Too high eddy viscosity of RANS

turbulence models is often blamed as a cause for a lack of cavitation *dynamics* in unsteady simulations of sheet cavitation (see, for example, Li et al., 2014), and has resulted in the development of *ad hoc* corrections to reduce the level of modelled viscosity close to the cavity surface (see, for example Coutier-Delgosha et al., 2003). In the present case, we see a large increase in the level of the eddy viscosity with grid refinement, particularly on the cavity surface. Although this does not prevent cavitation inception at the location reported here, further downstream the negative effect may be larger, and should be investigated further.

6 ADAPTIVE GRID REFINEMENT

Having examined the effect of grid refinement using a series of geometrically similar grids, we now investigate the potential of adaptive grid refinement to improve the prediction of tip vortex cavitation. This is motivated by large differences in the observed tip vortex cavity extent (compared to sheet cavity) as grid density increases, and a desire to achieve a similar improvement using fewer total grid cells.

6.1 AGR settings

The adaptive grid capabilities in ReFRESH allow a number of static and dynamic types of grid refinement and coarsening, depending on the flow problem. The refinement is based on an anisotropic division of cells marked for refinement, resulting in a new unstructured grid containing hanging nodes. Due to the stationary nature of the test case, a static refinement was made, similar to that reported by Windt & Bosschers (2015) for a non-cavitating tip vortex. This implies that the refinement is carried out only once, and the resulting grid used for a new computation without dynamic refinement.

Three helices of equal form were specified, each defining a tube-like shape within which cells were refined. The radius of the tube was successively decreased, with the smallest radius estimated from a non-cavitating computation on $G3$ by visualising an isosurface of the Q -criterion equal to unity, where $Q = \frac{1}{2} \left(\frac{\|\Omega\|^2}{\|\mathbf{S}\|^2} - 1 \right)$, with Ω and \mathbf{S} the rota-

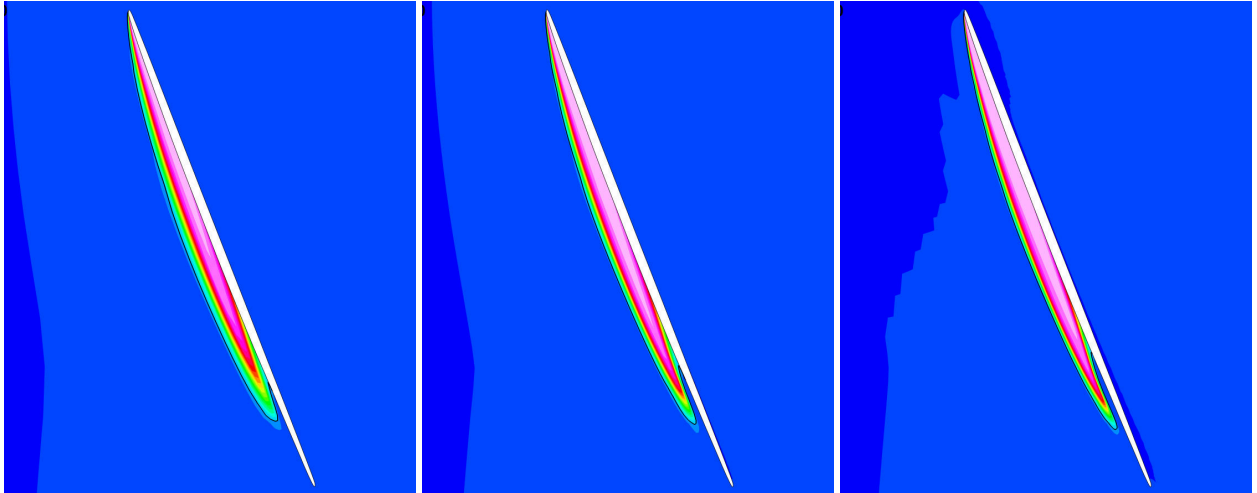
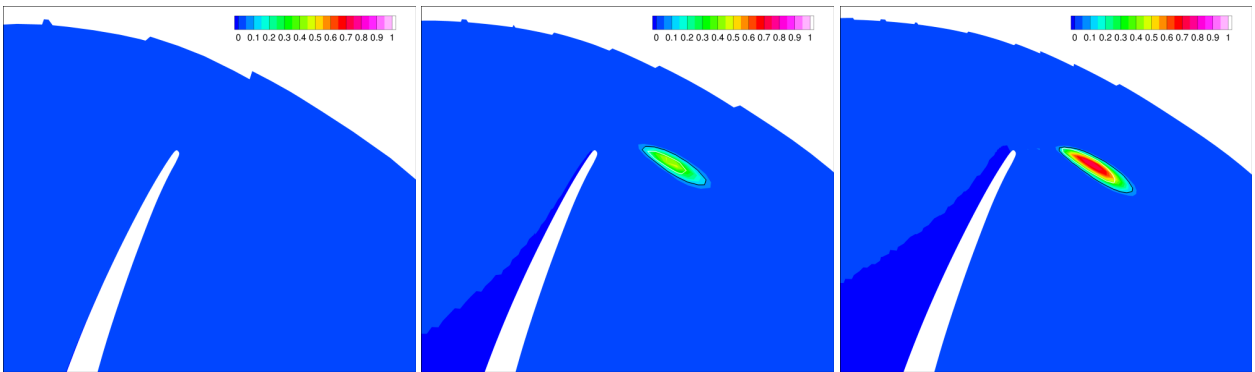
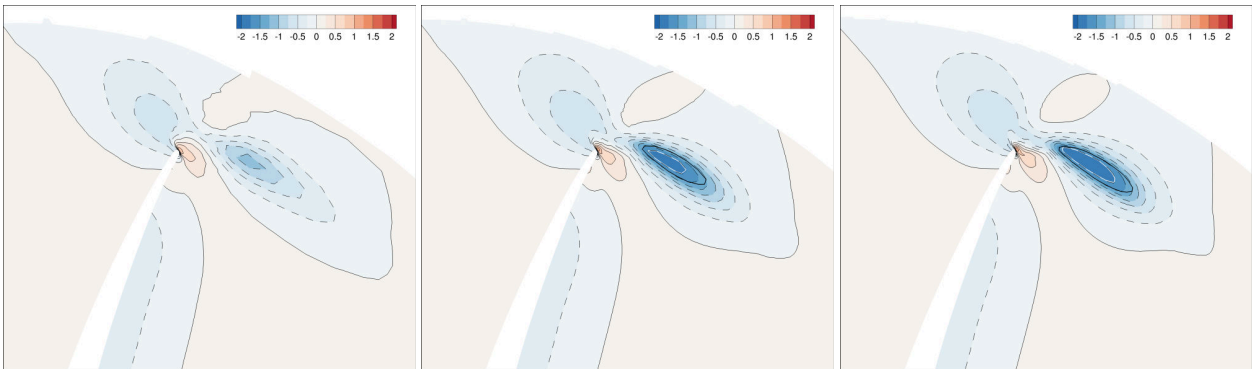


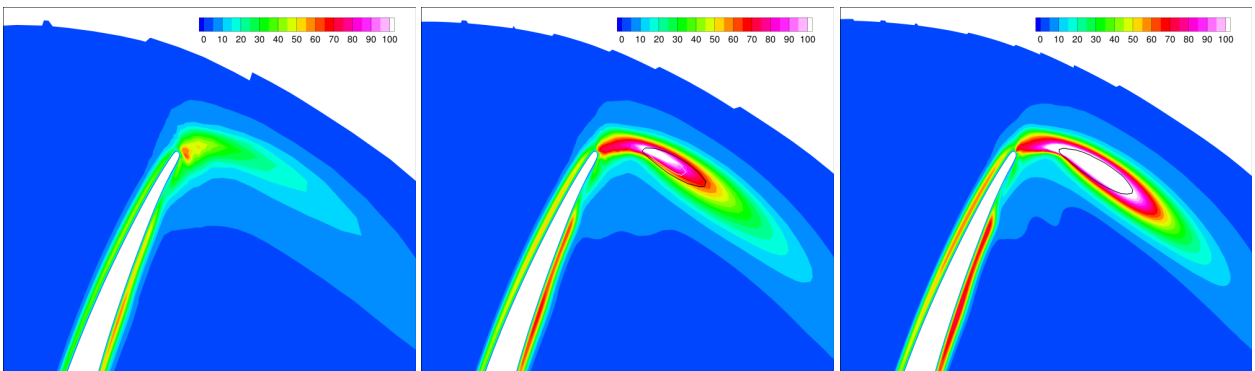
Figure 9: Contour of vapour volume fraction α_v at $r/R = 0.9$ (0: blue; 1: white). *G5* (left); *G3* (middle); *G1* (right).



(a) Vapour volume fraction α_v



(b) Pressure coefficient C_{pn}

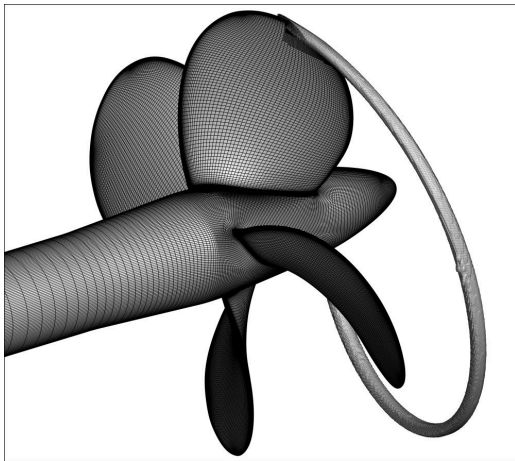


(c) Eddy viscosity ratio μ_t/μ

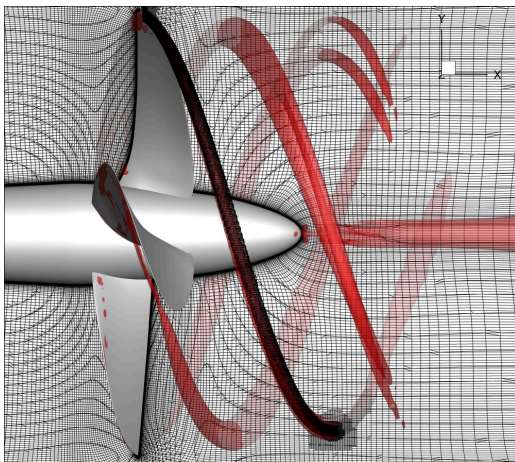
Figure 10: Axial slices downstream of propeller plane at $x/D = 0.05$. Isolines of $\alpha_v = 0.1$ (black) and $C_{pn} = -\sigma_n$ (white) also included. *G5* (left); *G3* (middle); *G1* (right).

tion and strain rate tensors. The resulting radii for the three helices were approximately equal to 4%, 2% and 1% of the propeller diameter. Helix pitch and downstream axial extent were defined as $(P/D)_{0.9R} \times D \times J$ and $0.5D$. Contraction of the tip vortex was also accounted for. Figure 11 shows views of the smallest helix.

This procedure was applied to a single blade (owing to the axisymmetric nature of the flow), with the aim of keeping the total number of cells below that of $G1$, while achieving a similar improvement in the prediction of the cavitation extent. $G3$ was chosen considering it to be a typical medium density grid, where the differences in propeller loading compared to finer grids were small, yet the cavitating tip vortex had only partially been captured. Since the grid refinement ratio between $G3$ and $G1$ was approximately 1.5, a single level of AGR was sufficient to achieve a similar cell size inside the tip vortex as $G1$. This grid is referred to as $A1$ and contained $0.4 M$ additional cells. Results are also presented for the other refinement levels (denoted as $A2$ and $A3$ respectively) for which a total of $1.4 M$ and $3.2 M$ were added.



(a) perspective view



(b) side view with iso-surface of Q -criterion equal to unity

Figure 11: Views of adapted grid. The helix shown represents cells refined during the third refinement stage.

Computations using RANS and DDES were made in order to separate the effects of grid refinement and turbulence modelling on the cavitation prediction, resulting in all AGR simulations being run unsteady. The timestep was equivalent to one degree of rotation, which is coarse for cavitation simulations but considered sufficient for uniform inflow conditions. Computations were run for four propeller rotations using a steady flow solution as initial condition. The predicted forces and moments were all within 1% of the values from the steady computations.

6.2 AGR results

The results presented consist of similar analyses to those already shown in Figures 8 and 10. However, instead of showing only RANS results for three geometrically similar grids, we compare three levels of AGR for two turbulence modelling approaches. This is shown in Figure 12 for vapour extent, and Figures 14-15 for vapour volume fraction distribution, pressure coefficient and eddy viscosity ratio (on the same axial slice as Figure 10). The AGR level increases from left to right, with RANS and DDES results denoted using the suffixes R and D .

Differences between computations with and without AGR are clearly seen by comparing Figure 12 with results in Figure 8, where the tip vortex cavity is extended using AGR to a similar length to that seen for $G1$. As the local refinement level increases, not only does the TVC become longer, but the roll-up of the tip vortex is better captured (comparing to the experiment in Figure 1). When comparing the two turbulence modelling approaches, the DDES computations exhibit a longer TVC for all grids, due to the reduction in eddy viscosity with grid refinement, the opposite trend to that of RANS. Although the RANS and DDES computations using AGR both show similar predictions in terms of vapour volume distribution and pressure field, the DDES computations exhibit a more defined cavity shape, particularly for the coarse refinement levels. Larger regions of high α_v are also seen inside the cavity for DDES. Differences in the eddy viscosity contours are evident in Figure 15. AGR causes a significant increase in μ_t/μ in the tip vortex for RANS computations, more so than seen in Section 5. As expected the DDES computations result in a much lower level of μ_t/μ , including inside the cavity, since not all the turbulence is modelled. Examination of the pressure field further downstream of the slice location chosen here is required in order to fully reveal the effect of eddy viscosity level on the pressure field inside the vortex.

Finally, differences in predictions of the TVC volume and extent between different grids and turbulence models are summarised in Figure 16. The normalised vapour volume is defined as $V_v^* = V_v/A_0^{3/2}$, where V_v is the integrated TVC vapour volume and A_0 is a reference area equal to $0.46R^2$. Cavity axial extent is defined as $x^* = (x_{max} - x_0)/(P_{0.9R}J)$, with x_{max} the maximum axial ex-

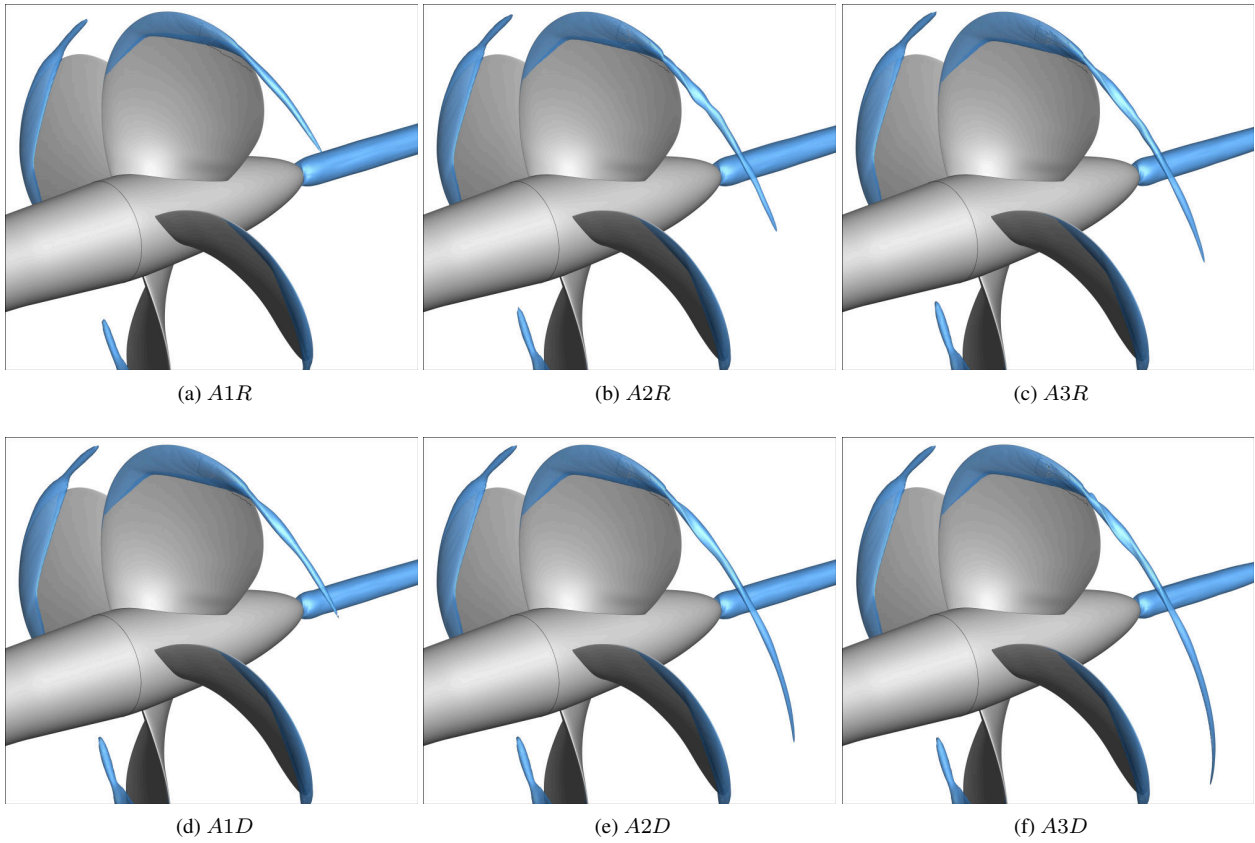


Figure 12: Cavity extents for different combinations of adapted grid and turbulence model. Cavity visualised using isosurfaces of the vapour volume fraction $\alpha_v = 0.1$.

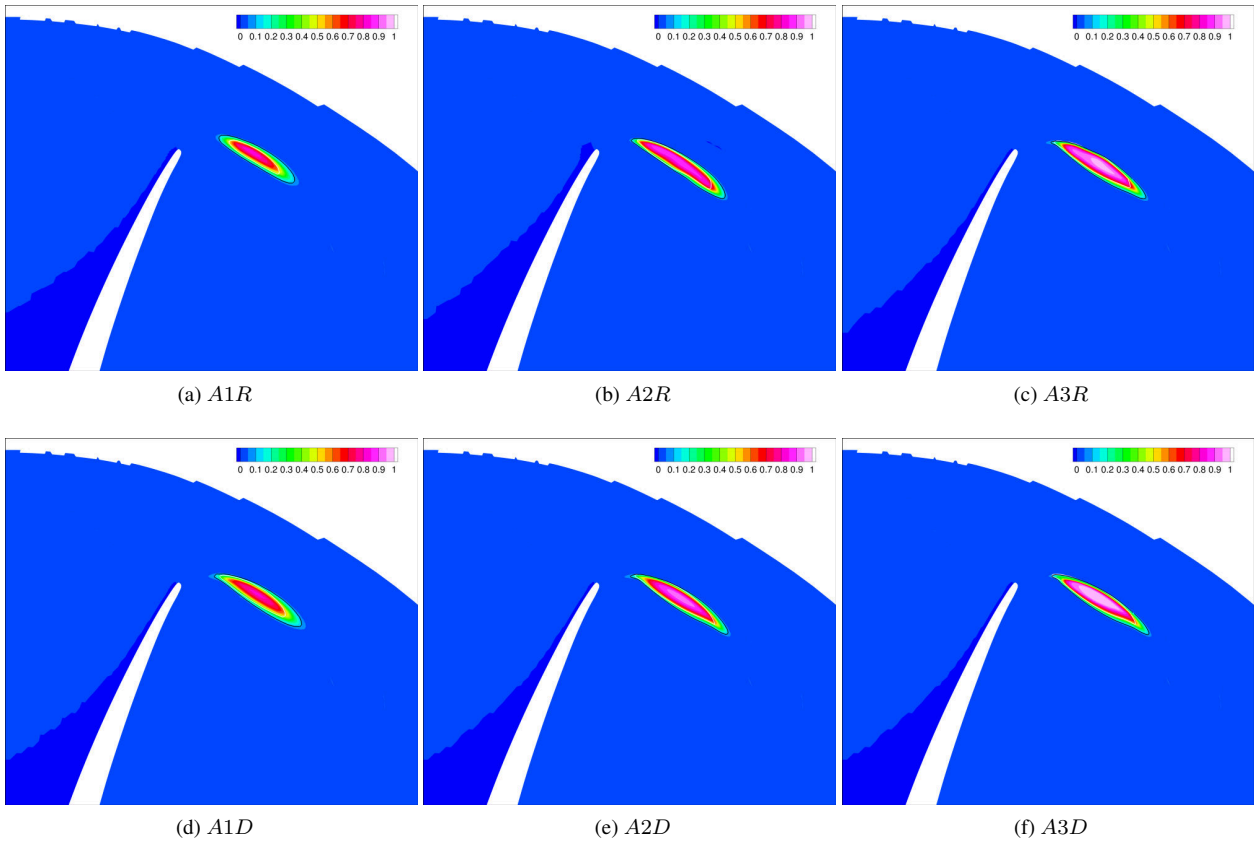


Figure 13: Axial slice of vapour volume fraction downstream of propeller plane ($x/D = 0.05$), for different combinations of adapted grid and turbulence model.

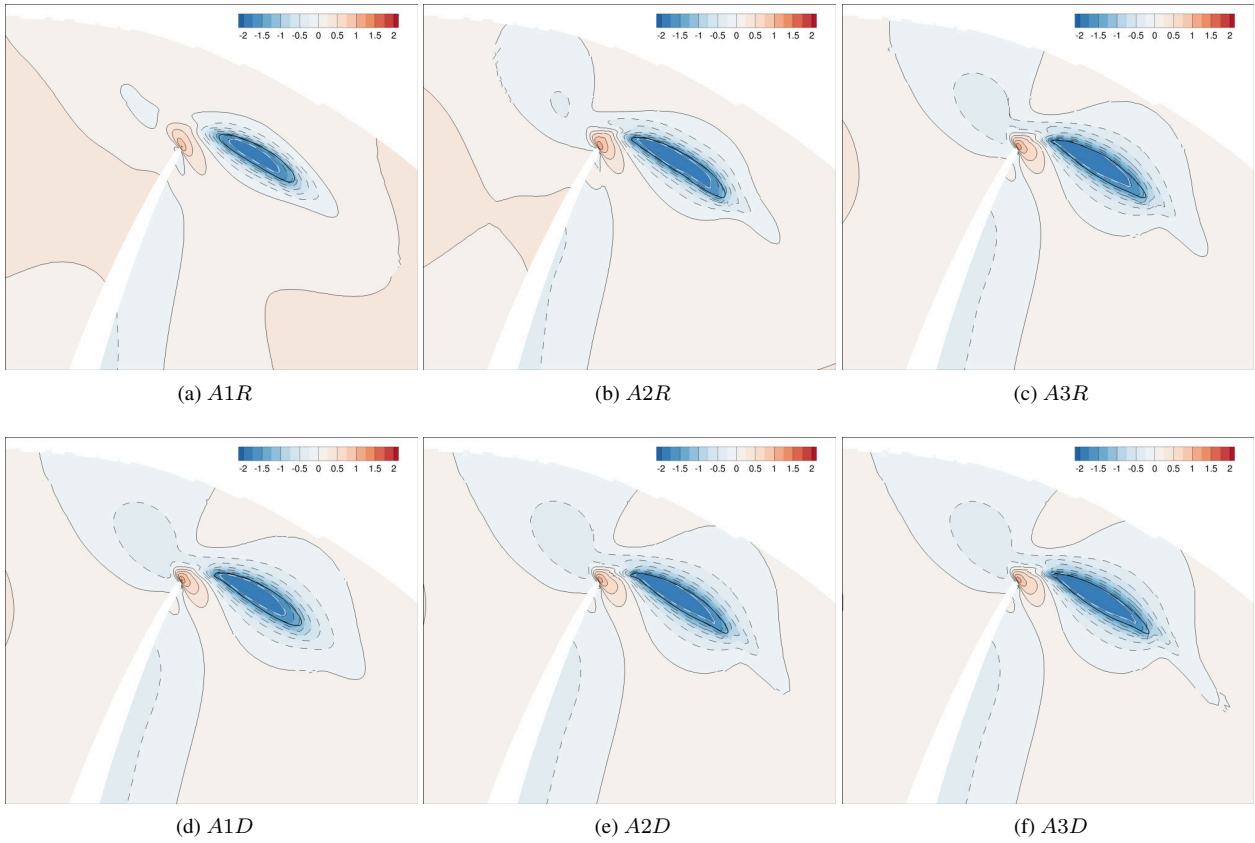


Figure 14: Axial slice of pressure coefficient C_{pn} downstream of propeller plane ($x/D = 0.05$) for different combinations of adapted grid and turbulence model.

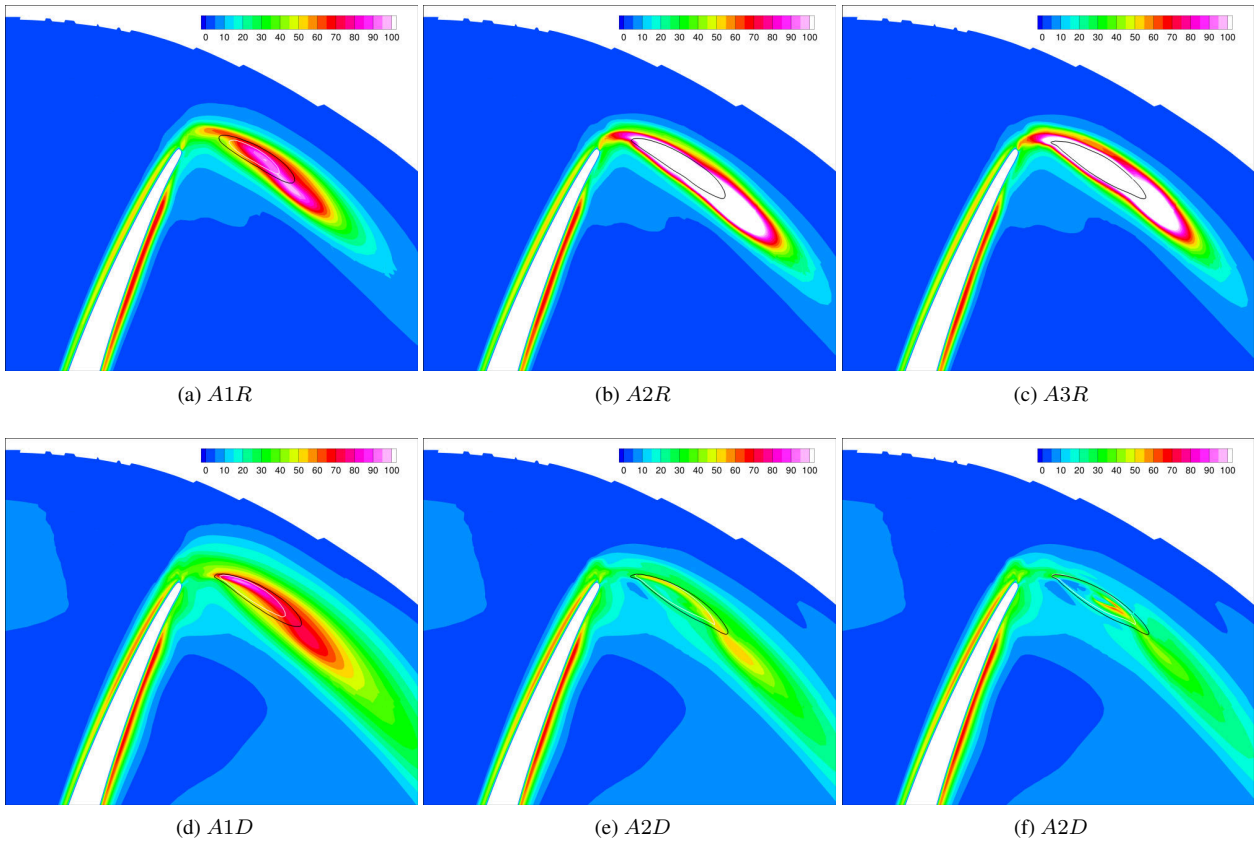


Figure 15: Axial slice of eddy viscosity ratio μ_t/μ downstream of propeller plane ($x/D = 0.05$), for different combinations of adapted grid and turbulence model.

tent of the cavity and x_0 the reference axial position corresponding to the start of the tip vortex. The typical cell size is given as the ratio with respect to $G3$ such that a finer grid results in a value larger than unity. Although for all computational approaches V_v^* and x^* increase with grid refinement, Figure 16 emphasises that DDES should be preferred to RANS for further studies of TVC using AGR. However, grid-independent results have not yet been obtained, meaning further refinement may be necessary in order to achieve sufficient activation of the LES-like behaviour of DDES. Note that the characteristic cell size for $A3$ is estimated to be around 120 times the Kolmogorov scale. Although this is 3-6 times larger than recommended in the literature, it is expected that the grid requirements for cavitating computations are somewhat less onerous than non-cavitating due to the equalised pressure inside the cavitating vortex.

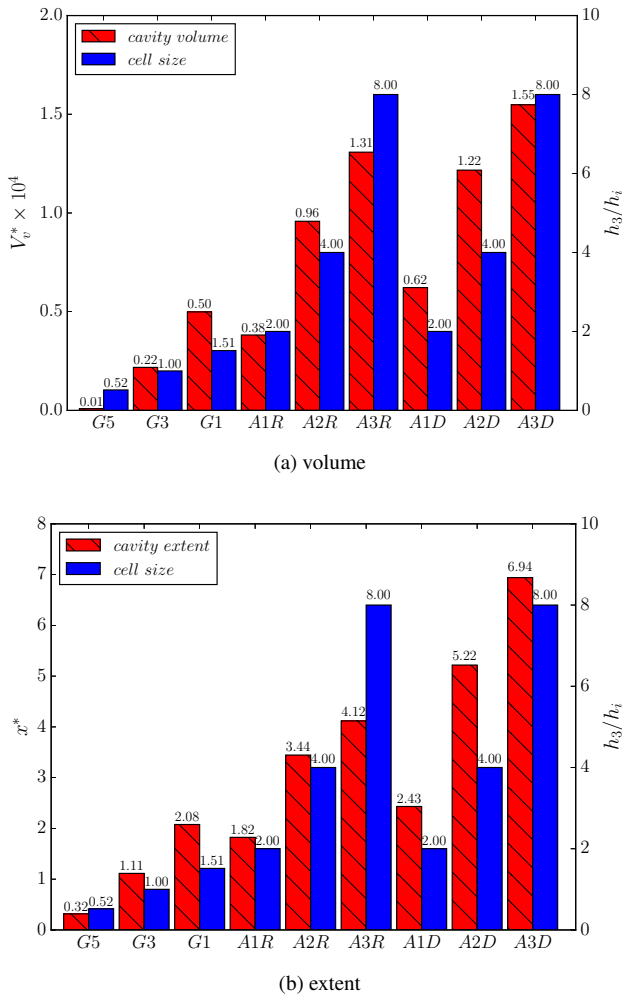


Figure 16: Differences in tip vortex cavity volume and extent between grids. Typical cell size indicated as ratio with respect to $G3$, denoted as h_3/h_i .

7 CONCLUDING REMARKS

In this study the effect of grid density and topology on cavitating propeller flow predictions was investigated. Using steady RANS computations on geometrically similar struc-

tured grids, an uncertainty analysis of cavitating propeller CFD was made for the first time. Furthermore the use of adaptive grid refinement to locally improve the resolution of tip vortex cavitation was also investigated. The work leads to the following conclusions:

- The grid uncertainty of both wetted and cavitating propeller computations in uniform flow is low. In this case (high rotation rate), the thrust and torque values are dominated by the pressure component, which is relatively grid insensitive. The wetted flow computations show more grid sensitivity due to the improvement in the resolution of the leading edge vortex with grid refinement, a feature which is much weaker for the cavitating flow condition.
- Performance coefficients for cavitating flow computations show a much lower order of convergence than wetted flow (which approach or reach the maximum theoretical value). It is also noted that the iterative convergence for the cavitating flow cases was not as good as for wetted flow, something which could be studied further in future work.
- Although thrust breakdown was expected for the cavitating condition based on the experimentally measured forces, this was not observed in the simulations. This has been attributed to the overprediction of the sheet cavitation extents, which compensate the reduction in thrust due to the weaker leading edge vortex. This is likely due to assumptions in the flow modelling, namely fully turbulent flow and the simplified cavitation inception criterion $p < p_v$.
- Although grid refinement did not have a large effect on the sheet cavity extent, the cavity interface became thinner for finer grids, with a high concentration of vapour inside the cavity and a more pronounced cavity tail. As expected, grid density was seen to be very important for tip vortex cavitation, where the minimum pressure inside the vortex reduced significantly as the grid was refined. From a grid where no tip vortex cavitation was predicted ($G5$), a grid refinement ratio of approximately 2.4 was sufficient for a reasonably extended tip vortex to develop ($G1$).
- The benefit of applying *a priori* adaptive grid refinement in the region of the tip vortex was clearly demonstrated as being beneficial for tip vortex cavitation prediction, although this was also sensitive to turbulence model. Use of AGR allows a similar prediction of the cavity extent as seen for a finer grid, while using fewer total grid cells. Furthermore the details of the tip vortex roll-up were better captured using AGR.
- For the adapted grids, the much finer cells inside the tip vortex lead to significant increases in eddy viscos-

ity when using RANS, which even lead to reduction of the predicted cavity extent compared to DDES. This leads to the conclusion that RANS is not suitable for TVC prediction, especially when the focus is on dynamics.

Future work should focus on the extension of the uncertainty analysis to unsteady (DDES) simulations. This will allow the effect of timestep to be included in the verification analysis. It is expected that timestep is less important than grid density, based on the current study, although it will be important to study its effect on cavity fluctuations. The results using AGR could also be extended to a full grid uncertainty analysis, as was done for a non-cavitating propeller by Windt & Bosschers (2015).

REFERENCES

- Asnaghi, A., Feymark, A. & Bensow, R. E., 2016. 'Numerical analysis of tip vortex flow'. Proceedings of 19th Numerical Towing Tank Symposium. 3rd-4th October, St. Pierre d'Oléron.
- Coutier-Delgosha, O., Reboud, J. L. & Delannoy, Y., 2003. 'Numerical simulation of the unsteady behaviour of cavitating flows'. International Journal for numerical methods in fluids, **42**, pp. 527–548.
- Decaix, J., Balarac, G., Dreyer, M., Farhat, M. & Münch, C., 2015. 'RANS computations of tip vortex cavitation'. Proceedings of 9th International Symposium on Cavitation. 6th-10th December, Lausanne.
- Eça, L. & Hoekstra, M., 2014. 'A procedure for the estimation of the numerical uncertainty of CFD calculations based on grid refinement studies'. Journal of Computational Physics, **262**, pp. 104–130.
- Gaggero, S., Tani, G., Viviani, M. & Conti, F., 2014. 'A study on the numerical prediction of propellers cavitating tip vortex'. Ocean Engineering, **92**, pp. 137–161.
- Gritskevich, M. S., Garbaruk, A. V., Schütze, J. & Menter, F. R., 2012. 'Development of DDES and IDDES formulations for the $k-\omega$ shear stress transport model'. Flow, Turbulence and Combustion, **88**(3), pp. 431–449.
- Li, Z., Pourquie, M. & van Terwisga, T., 2014. 'Assessment of cavitation erosion with a URANS method'. Journal of Fluids Engineering, **136**(4), p. 041101.
- Lloyd, T. P., Rijpkema, D. R. & van Wijngaarden, E., 2015. 'Propeller acoustic modelling: comparing CFD results with an acoustic analogy approach'. Proceedings of the 4th International Symposium on Marine Propulsors. 31st May-4th June, Austin.
- Menter, F. R., Egorov, Y. & Rusch, D., 2006. 'Steady and unsteady flow modelling using the $k-\sqrt{k}L$ model'. Proceedings of the International Symposium on Turbulence, Heat and Mass Transfer, pp. 403–406.
- Negrato, C., Lloyd, T. P., van Terwisga, T., Vaz, G. & Bensow, R., 2017. 'Numerical study of cavitation on a NACA0015 hydrofoil: solution verification'. Proceedings of the 7th International Conference on Computational Methods in Marine Engineering. 12th-5th May, Nantes, pp. 1–12.
- Reverberi, A., Lloyd, T. P. & Vaz, G., 2016. 'Cavitation modelling accounting for transition effects'. Wackers, J. (ed.) Proceedings of 19th Numerical Towing Tank Symposium. 3rd-4th October, St. Pierre d'Oléron.
- Rijpkema, D. R., Baltazar, J. & Falcão de Campos, J., 2015. 'Viscous flow simulations of propellers in different Reynolds number regimes'. Proceedings of the 4th International Symposium on Marine Propulsors. 31st May-4th June, Austin.
- Rijpkema, D. R. & Vaz, G., 2011. 'Viscous flow computations on propulsors: verification, validation and scale effects'. Proceedings of Marine CFD. London.
- Salvatore, F., 2007. 'The INSEAN E779A propeller experimental dataset'. Tech. rep., INSEAN, Report No. D4.1.3.
- Sauer, J. & Schnerr, G. H., 2001. 'Development of a new cavitation model based on bubble dynamics'. Zeitschrift für Angewandte Mathematik und Mechanik, **81**(S3), pp. 561–562.
- Vaz, G., Hally, D., Huuva, T., Bulten, N., Muller, P., Becchi, P., Herrero, J. L. R., Whitworth, S., Mace, R. & Korsström, A., 2015. 'Cavitating flow calculations for the E779A propeller in open water and behind conditions: code comparison and solution validation'. 4th International Symposium on Marine Propulsors. 31st May-4th June, Austin, pp. 330–345.
- Wang, B., Liu, Z., Peng, X. & Liu, D., 2015. 'Simulations of tip vortex cavitation flows with nonlinear $k-\epsilon$ model'. Proceedings of 9th International Symposium on Cavitation. 6th-10th December, Lausanne.
- Windt, J. & Bosschers, J., 2015. 'Influence of local and adaptive mesh refinement on the tip vortex characteristics of a wing and propeller'. Salvatore, F., Broglia, R. & Muscari, R. (eds.) Proceedings of the VI International Conference on Computational Methods in Marine Engineering. Rome, pp. 1–12.
- Yvin, C. & Muller, P., 2016. 'Tip vortex cavitation inception without a cavitation model'. Wackers, J. (ed.) Proceedings of 19th Numerical Towing Tank Symposium. 3rd-4th October, St. Pierre d'Oléron.